iScience

CellPress
OPEN ACCESS

Article

Design of a long-lived Mo2C-MoO2@GC-N electrocatalyst by the ambient DC arc plasma for the hydrogen evolution reaction

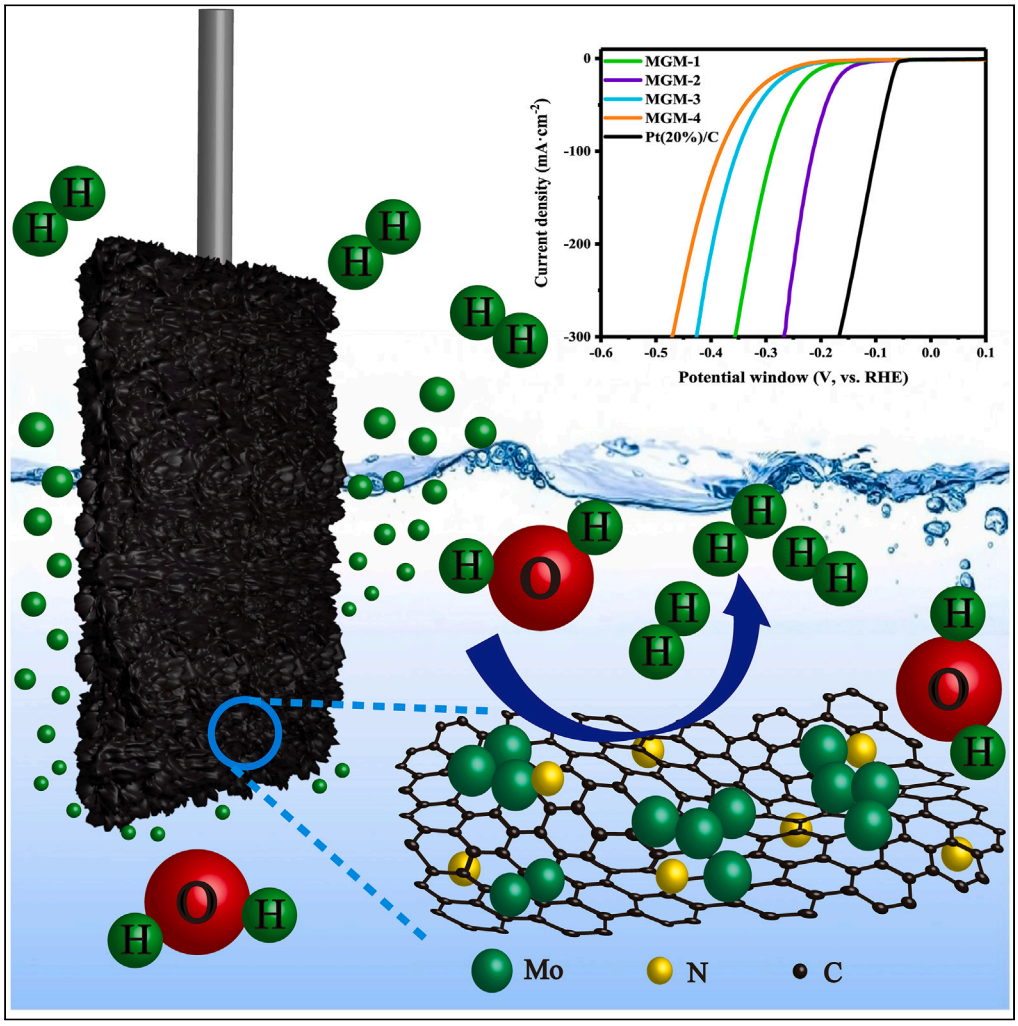

Marian Chufarov, Yuliya Z. Vassilyeva, Xinyu Zhang, Shilin Li, Alexander Y. Pak, Wei Han

zhangxy3@sustech.edu.cn (X.Z.)
ayapak@tpu.ru (A.Y.P.)
whan@jlu.edu.cn (W.H.)

Highlights

The Mo-based electrocatalysts for H_2 evolution were prepared by DC arc discharge plasma

Nitrogen-doped Mo_2C-MoO_2@GC composites exhibited superior HER in alkaline media

The overpotentials of 148 mV for HER at a current density of 10 mA·cm^{-2}

High catalytic activity remains well even after 15 days of continuous electrolysis

Chufarov et al., iScience 27, 110551
September 20, 2024
https://doi.org/10.1016/j.isci.2024.110551

iScience

CellPress
OPEN ACCESS

Article

Design of a long-lived Mo2C-MoO2@GC-N electrocatalyst by the ambient DC arc plasma for the hydrogen evolution reaction

Marian Chufarov,[1,4] Yuliya Z. Vassilyeva,[1,2,4] Xinyu Zhang,[3,*] Shilin Li,[1] Alexander Y. Pak,[2,*] and Wei Han[1,5,*]

SUMMARY

A crucial challenge in hydrogen production through electrolysis is developing inexpensive, earth-abundant, and highly efficient Pt-free electrocatalysts for the hydrogen evolution reaction (HER). Molybdenum carbide is ideal for this application because of its special electrical structure, low cost, and advantageous characteristics. Herein, the long-lived electrocatalysts for HER have been synthesized via the direct current (DC) arc discharge plasma method under ambient air conditions, and the relationship between the properties of materials and catalytic characteristics has been established. The samples differed in the ratio of molybdenum, graphite, and melamine. The sample with the highest proportion of melamine in the initial mixture has Mo2C-MoO2 heterointerfaces, which demonstrates the highest and most stable electrocatalytic activity with the overpotential of 148 mV at 10 mA·cm^{-2} and Tafel slope of 63 mV·dec^{-1} in alkaline electrolyte. Meanwhile, the electrodes demonstrated long-lived electrochemical durability for two weeks and investigated the features of forming a stable system for HER.

INTRODUCTION

Because the process of generating energy is unstable or unexpected, a significant amount of energy obtained from renewable sources, such sunlight or wind, may be lost permanently. The conversion by means of the water-splitting process is one of the ways to conserve such energy.[1,2] Hydrogen is a clean and versatile energy carrier and could become an important element of the future fuel mix in various industries, reducing humanity's dependence on fossil energy sources. In addition, hydrogen derived from renewable energy can provide a critical link between electricity generation from renewable sources and sectors with difficulties in decarbonization, such as industry and heavy transport.[3]

One of the most promising methods for producing hydrogen on a practically large scale and at a cheap cost is electrochemical water splitting.[4,5] The two reactions involved in electrochemical water splitting are the oxygen evolution reaction (OER) on the anode and the hydrogen evolution reaction (HER) on the cathode. Because of inevitable dynamic overpotentials in both reactions, an electrocatalyst is needed to reduce the reaction energy barriers.[6,7] At the moment, compounds based on platinum (Pt) and palladium (Pd) exhibit the highest catalytic activity toward HER.[8,9] However, its limited availability and expensive cost prevent it from being used widely.[10,11] Therefore, the overpotential is greatly reduced for increased efficiency by utilizing a noble-metal-free electrocatalyst with low cost, high activity, high surface area, and high stability.

Many electrocatalysts based on transition metal carbides with outstanding electrochemical performance for HER have been reported recently.[12–19] Among them, molybdenum carbides are a good replacement for platinum due to their excellent catalytic activity and high stability in acidic and basic mediums.[20–22] It was found that the Mo_2C phase is more active than other ones due to its special electronic structure, which is similar to the electronic states of Pt.[23,24] Moreover, Mo_2C particles encapsulated inside carbon layers as carbon nanotubes (CNT), reduced graphene oxide (RGO), and carbon-fiber paper have enhanced electrochemical activity and stability.[25–27] Furthermore, because heteroatoms and carbon undergo charge transfer, non-metallic elements like N, P, B, and so forth in a carbon matrix can control the electronic structure and hydrogen adsorption strength of carbon.[28] For example, Mo_2C combined with reduced graphene oxide forms the Mo_2C@NPC/NPRGO nanocomposite catalyst synthesized by simple two-step impregnation-calcination, which exhibits excellent for HER superior to commercial Pt/C in acidic electrolyte.[29] Besides, previous investigations have shown that the introduction of various transition metals (TM) such as Fe, Ni, Co, Cu, and Zn has successfully promoted the hydrogen evolution electrocatalytic activity of carbide-based composites.[30–33] Wang et al.[34] synthesized the Mo_2C-NC@Co_xFe_y catalyst by pyrolysis of cobalt ferrite coated with cross-linked melamine-formaldehyde molybdic acid resin. The resulting composite was Co_xFe_y alloy nanoparticles in N-doped graphene shells containing additional molybdenum carbide

[1]College of Physics, the State Key Laboratory of Inorganic Synthesis and Preparative Chemistry, International Center of Future Science, Jilin University, Changchun 130012, China
[2]Laboratory of Advanced Materials for Energy Industry, Tomsk Polytechnic University, Tomsk 634050, Russian Federation
[3]Department of Physics, Southern University of Science and Technology, Shenzhen 518055, China
[4]These authors contribute equally
[5]Lead contact
*Correspondence: zhangxy3@sustech.edu.cn (X.Z.), ayapak@tpu.ru (A.Y.P.), whan@jlu.edu.cn (W.H.)
https://doi.org/10.1016/j.isci.2024.110551

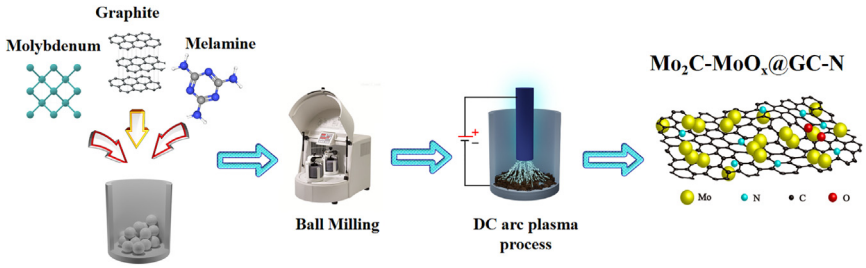

Figure 1. A schematic illustration of the formation of the $Mo_2C@MoO_2$ and $Mo_2C@MoO_2@Mo$ composites

nanoparticles and exhibited excellent HER performance in alkaline media.[34] Recently, surface modification of Mo_2C and the creation of Mo_2C-TMO heterostructures or heterointerfaces had beneficial effects on the electrochemical performance of molybdenum carbide in various applications.[35–37] Due to the fact that heterostructures made of transition metal oxide and molybdenum carbide may efficiently control the electrical configuration, the process of producing hydrogen can be accelerated considerably. Ni et al.[38] synthesized by a solvothermal-assisted self-assembly procedure molybdenum carbide doped NiO, which has modified the electron density on the surface of Mo_2C and demonstrated a synergistic effect with RGO, thereby exhibiting improved electrocatalytic performance of NiO/β-Mo_2C/RGO catalysts in acidic and alkaline electrolytes. In 2020, He et al. produced a heterogeneous MoO_2-Mo_2C structure on the surface of pyrolytically produced Mo_2C/CC on carbon fabric by RF plasma (150 W) under O_2. Further electrochemical testing revealed that the excellent electrocatalytic HER activity in 1M $HClO_4$ is provided by the *in situ* transition of Mo (VI) to Mo (IV) species at Mo_2C-MoO_2.[39] Because previous results indicate that coupling Mo2C particles and Mo2-MoO2 heterostructures with nanocarbons is an excellent strategy to improve HER activity: firstly, carbon substrates create a path for rapid electron transfer without resistance, and also effectively inhibit the aggregation of Mo2C nanoparticles[40]; secondly, bonding conjugation can shift the center of the molybdenum d-band downward, causing charge transfer from molybdenum to carbon, thus achieving a relatively moderate Mo-H bond strength for enhanced H desorption.[41] However, most known methods involve complex or dangerous synthetic procedures and expensive precursors, making their practical application difficult. Nowadays, the following methods are used: solid-state reaction method,[42–44] mechanochemical synthesis,[45] calcination,[46] temperature reduction method,[47] wet impregnation method,[48] laser ablation,[36,49] arc discharging in inert and liquid medium,[50–52] carburization,[53] etc. Recently, the DC arc discharge method was successfully applied for different carbide syntheses, including molybdenum carbide.[54–59]

In this regard, we present a study of designed Mo_2C-based composites with heterointerfaces obtained by the DC arc discharge method in ambient air with simplifying system design as effective electrocatalyst materials for hydrogen production in alkaline media. During a targeted search for the optimal ratio of starting components for the synthesis of a catalyst based on molybdenum carbide to obtain maximum activity and stability of properties, the formation of two types of heterointerfaces based on Mo/MoO_2 and MoO_x on the surface of Mo_2C integrated into a graphitic carbon matrix doped with nitrogen was discovered. The resulting composite Mo_2C-MoO_2@GC-N is a highly active electrocatalyst for HER in alkaline media and also demonstrates an increased potential of only 17% after 15 days for the HER stability test.

RESULTS AND DISCUSSION

Figure 1 show the DC arc discharge process used to produce the Molybdenum, Graphite, Melamine (MGM) samples. The method's primary benefit is that it can be used in an open environment without requiring pumps, protective gases, or a vacuum chamber. The self-shielding system of CO_x gases, which partially prevents the synthesizing product from oxidation, is created between the electrodes during the arcing. Hence, this approach simplifies system design and reduces synthesis costs. The special shape and arrangement of the electrodes provide maximum energy input into the system, because the arc discharge passes directly through the starting mixture. According to the current and voltage waveforms obtained by an oscillograph, the input energy and discharge power were equaled to 40 $\pm$ 0.5 kJ and 4 $\pm$ 0.05 kW in each experiment, respectively. According to the obtained data, more than one crystalline phase is simultaneously present in the synthesized product, including molybdenum carbide, and it seems to be a completely normal phenomenon, as well as immersion of molybdenum carbide particles into a carbon matrix.[27,60] The well-known C-Mo phase diagram explains how an excess of carbon during synthesis leads to creating a carbon matrix.[61] This carbon matrix can efficiently reduce aggregation and make it easier to build molybdenum carbide with a distinct nanostructure, revealing many active sites and improving HER performance.[62]

X-ray diffraction (XRD) was used to examine the phase composition of the produced samples in the 2θ range of 10–70°, the matching patterns are displayed in Figure 2A. For all samples, the main peak located at about 26.4° corresponds to the (002) reflex of the graphitic crystal structure (Figure 2B). Diffraction peaks characteristic of a graphite grating in the 2θ range 42–45° (superposition of reflections (100) and (101)) are usually very weak (ISCD #96-901-2231[63]), as is observed in our case (Figure 2C). The peak of about 26.2° is also clearly observed (Figure 2B) due to the presence of the crystalline phase of MoO_2. As you can see in Figure 2C, the formation of MoO_2 is confirmed by reflections at 34 and 72° (ICSD # 96-154-8821,[64]). Diffraction reflections around 34.6, 38.0, 39.6, and 52.3° are consistent with the existence of Mo_2C (ISCD # 96-591-0010,[65]) for all samples (Figure 2C). In addition, metal molybdenum was found in samples MGM-3 and MGM-4 (Figure 2C, ISCD # 96-400-1309;[66]). Semi-quantitative XRD of crystalline phases was performed using the "reference intensity ratio"(RIR)-method in Match!3 software.[67] The results of the analysis are presented in Table S1. The amount of the graphite-like phase dominates in all samples and ranges from 84 to 94% wt. A significant

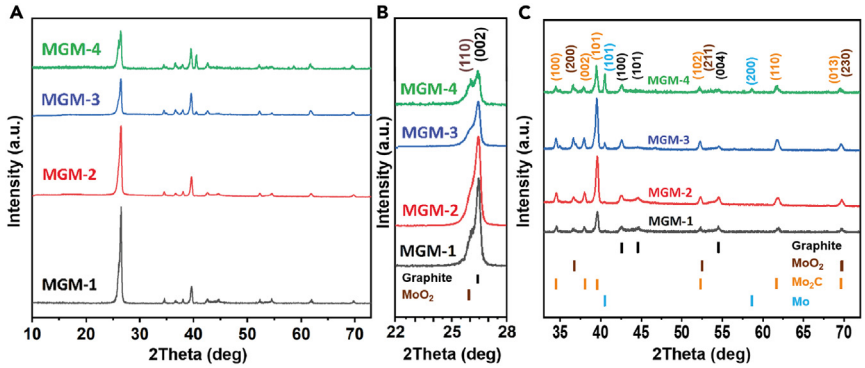

Figure 2. XRD patterns of synthesized MGM samples

(A) Region of 2θ = 10–73°.

(B) Increased region of 2θ = 22–28°.

(C) Increased region of 2θ = 34–60°.

decrease in the products of the interaction of molybdenum indicates that the transformation occurs simultaneously along several routes. First, a significant proportion of molybdenum evaporates due to the formation of volatile MoO_3 during synthesis in the open air. Second, the presence of a reducing atmosphere (CO and products of thermal decomposition of melamine) leads to the production of MoO_x ($x < 3$), in our case MoO_2. Since the melting point of MoO_3 (795°C) is lower than the melting point of MoO_2 (1135°C), so MoO_3 will evaporate from the composite during the synthesis of the sample in air. Molybdenum dioxide MoO_2 has good electronic conductivity ($8.8 \times 10^{-5}\ \Omega\ cm^{-1}$ in bulk samples at 300 K) and excellent chemical stability, which serve as active sites that have higher H coverage and lead to great potential in HER performance.[68,69] In addition, part of the molybdenum reacts with carbon and is converted to Mo_2C. It should be noted that an increase in the amount of molybdenum in the initial mixture leads to its incomplete transformation. Thus, 0.7 and 3.3% wt. metallic molybdenum was found in the synthesis products of MGM-3 (initial ratio Mo/Graphite = 1.5) and MGM-4 (initial ratio Mo/Graphite = 2.0) (Table S1).

As can be seen from SEM photographs (Figures 3 and S1), there is an uneven distribution of molybdenum carbide particles on the surface of the graphite matrix due to the high-temperature gradient in the arc formation zone, and the rate of its change is further from the discharge, the lower the temperature. This means that some agglomeration of particles may occur, as can be seen from some mapping elements, and the shape of the particles will depend on the ratio of the initial components.

Samples MGM-1 and MGM-4 are characterized by a flaky particle shape. Moreover, the higher the graphite content, the more uniformly the flake particles are distributed in the sample. The shape of the particles is closer to spherical in the MGM-2 sample. As the fraction of melamine decreases to a minimum in the initial mixture of the MGM-3 sample, the particles of the synthesized powder get a needle shape. According to energy dispersive spectroscopy (EDS), the samples contain the following main elements: Mo, C, N, and O, as shown in Figure S2. The amount of carbon in all samples is more than 80%. As noted earlier, excess unbound carbon can appear due to electrode erosion during synthesis and/or a significant proportion of carbon in the initial mixture of components. The proportion of oxygen in the samples was

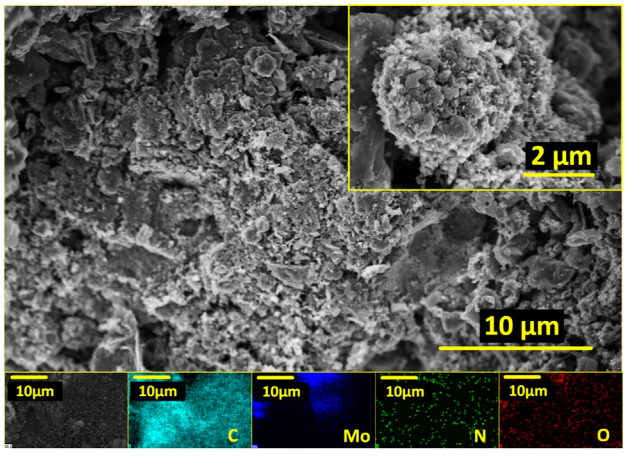

Figure 3. SEM images and elemental mapping of MGM-2 sample

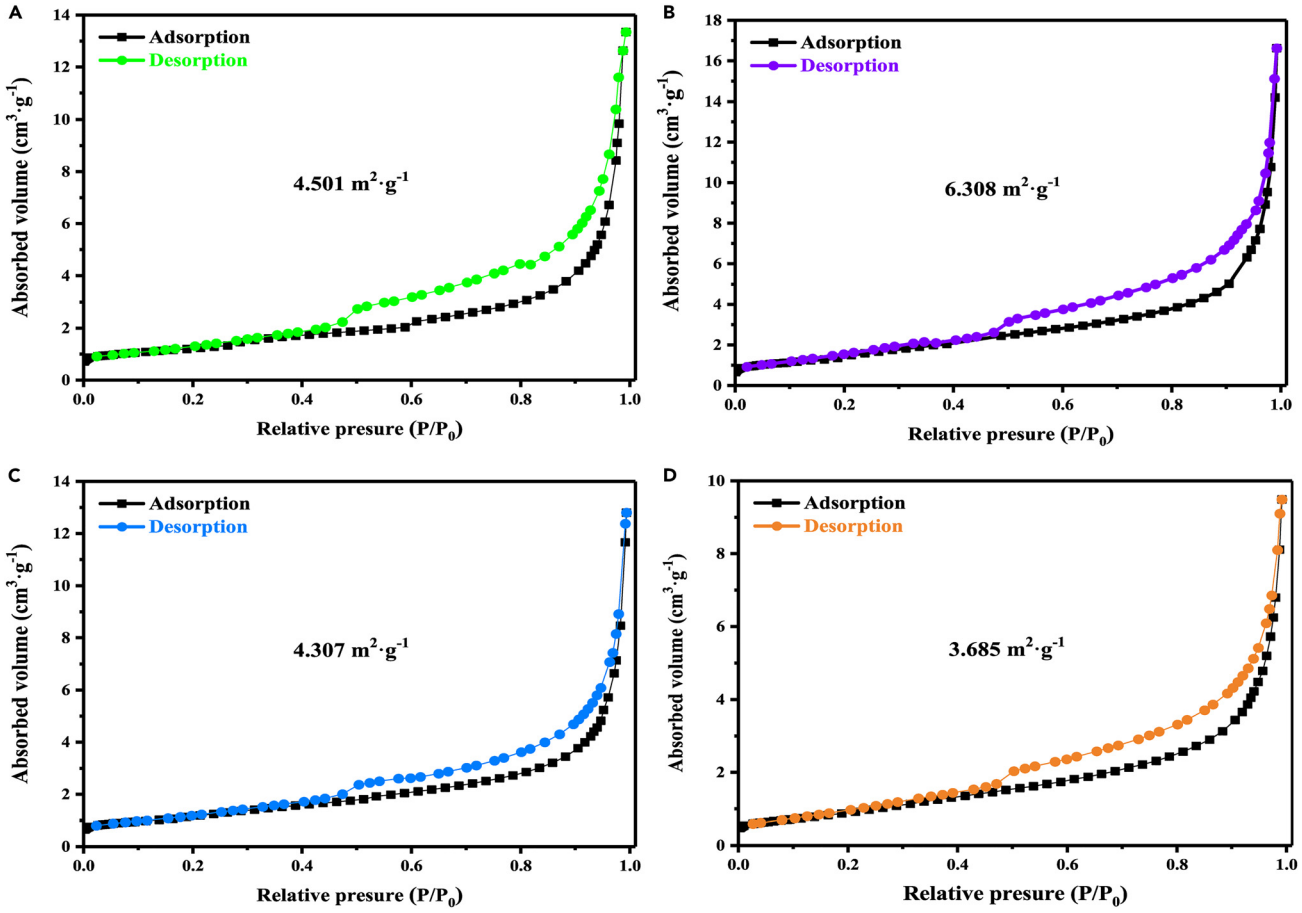

Figure 4. N_2 adsorption-desorption isotherms of MGM samples

(A) MGM-1 sample.

(B) MGM-2 sample.

(C) MGM-3 sample.

(D) MGM-4 sample.

determined by EDS (~5.0% wt.), which confirms the presence MoO_2 (Table S2). According to the EDS data, the MGM-2 sample has the highest amount of nitrogen (2.55% wt.).

The N_2 adsorption-desorption isotherms are shown in Figure 4. The isotherms belong to type IV isotherms because of a seen slope in the middle relative pressure region from 0.4 to 0.8.[62] The specific surface area calculated with the Brunauer-Emmett-Teller method for all samples is not so large. The MGM-4 sample has the smallest specific surface area (3.685 $m^2\ g^{-1}$), and the MGM-2 sample has the largest one—6.308 $m^2\ g^{-1}$. According to the pore size distributions presented in Figure S3, materials have a mesoporous structure with similar pore sizes of about 4 nm. Since large surface area is directly proportional to high electrocatalytic activity, it can be assumed that MGM-2 can exhibit the best HER performance. Therefore, the interface of the MGM-2 sample will be examined in more detail.

X-ray photoelectron spectroscopy (XPS) was used to further describe the MGM-2 sample in order to examine its composition and surface electronic state, as shown in Figure 5. The survey XPS spectra (Figure 5A), contain lines characteristic of molybdenum (5.71 at %), carbon (90.81 at. %), oxygen (2.21 at %), and nitrogen (1.27 at %). This outcome and the XRD data correlate quite well (Table S1). Narrow spectrum areas of the components present in the catalyst were also recorded, in addition to the survey photoelectron spectra. According to Figure 5B, the high-resolution Mo3d spectra consist of six peaks, which exhibit the presence of Mo species with three kinds of valence states. The peaks with a maximum of 231.9 eV and 228.5 eV correspond to $Mo3d_{5/2}$ and $Mo3d_{3/2}$ of Mo^{2+}, respectively, which indicates the presence of a molybdenum carbide.[70] Other peaks at binding energies of 234.1 eV and 229.8 eV are assigned to Mo^{4+} in MoO_2, and the intense peaks at 232.9 eV and 236 eV are attributed to Mo^{6+} in MoO_3.[71] Such high-oxidation states $Mo^{4+/6+}$ are formed due to slight passivation of the surface of molybdenum nanoparticles in air, which leads to the formation of MoO_2. Given that MoO_2 and MoO_3 are superior electron conductors, this may improve the catalytic activity of Mo_2C.[72] The high resolution of the C1s line shape is typical for graphite-like carbon bond (C=C/C–C) at 284.8 eV, C–N bond at 285.1 eV along with C–O bond at 287 eV, and Mo-C at 284.2 eV, which confirms the doping of the carbon lattice with N species and consistent with the expected structure of Mo_2C, as illustrated in Figure 5C.[60,73,74] The presence of C–N and C–O bonds

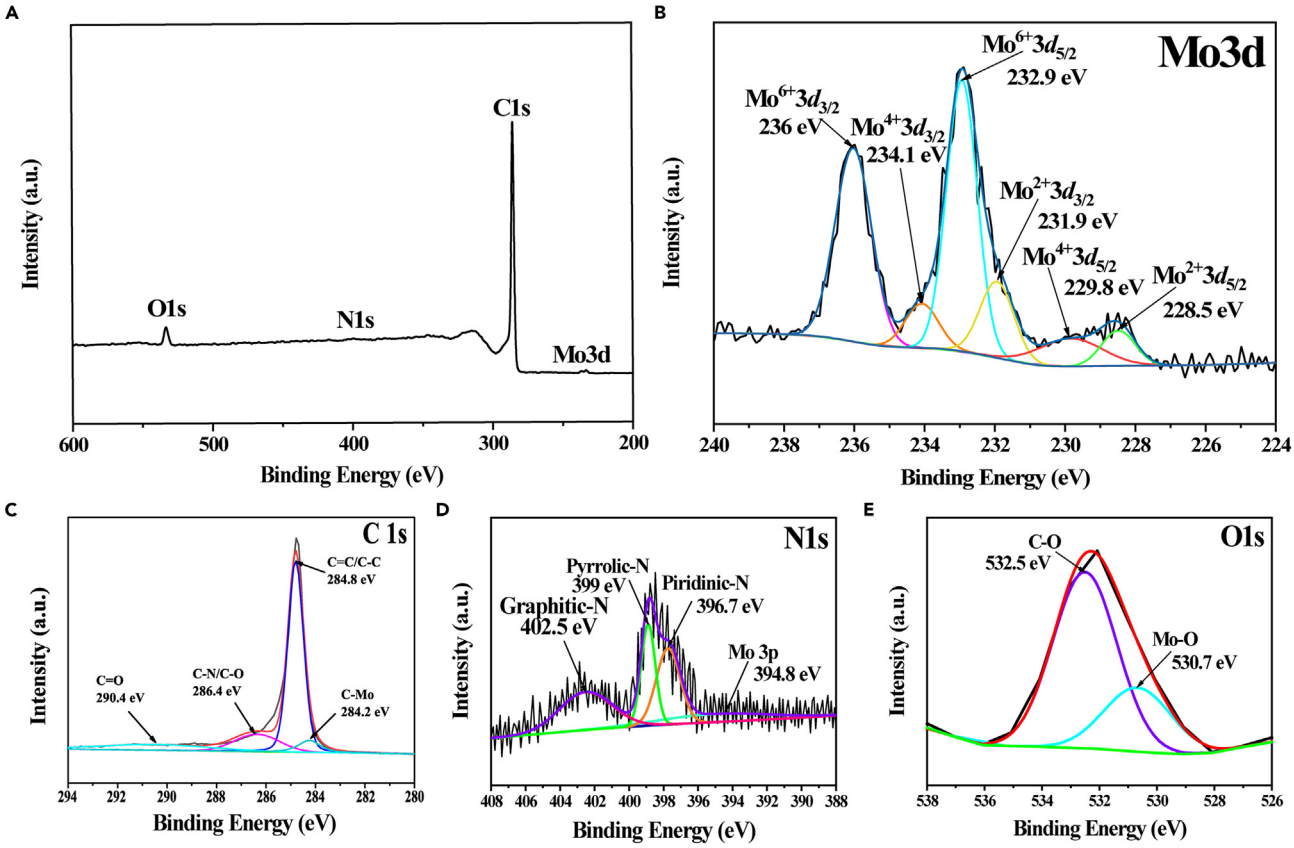

Figure 5. XPS spectrum and high-resolution XPS spectra for MGM-2 sample

(A) XPS survey spectrum.

(B) Mo3d.

(C) C1s.

(D) N1s.

(E) O1s spectra.

in the composite can lead to a synergistic effect, the oxygen-containing functional groups (C–O bonds) can facilitate electron transfer processes, complementing the catalytic activity of nitrogen-containing groups (C–N bonds).[75,76] In Figure 5D, the high-resolution N1s spectra can be decomposed into four peaks: graphitic-N (402.5 eV), pyrrolic-N (399 eV), pyridinic-N (396.7 eV), and Mo3p (394.8 eV).[77] The presence of the Mo3p peak confirms the relationship of Mo with N species, which are alloyed into a graphite carbon matrix.[78] Notably, the presence of nitrogen-containing groups (pyridinic, pyrrole, or graphitic nitrogen group) in carbon-based materials can provide active sites for HER catalysis, improving reaction kinetics.[75] Finally, the XPS spectra of the O1s region showed two peaks at 530.7 and 532.5 eV belonging to Mo–O bonds and C–O bonds, respectively, as shown in Figure 5E. The presence of a low-intensity peak of Mo–O bonds confirms the formation of MoO_2 due to oxidation of the surface of Mo nanoparticles upon contact with air.[58] The XPS results indicate the formation of Mo_2C-MoO_2 heterointerfaces on N-doped carbon matrix, which can positively affect the electrocatalytic.

From the transmission electron microscopic (TEM) image (Figure 6A), it can be observed that the sample has a lamellar nanosheet or film structure.[23] The size of the nanosheets is between 400 and 600 nm. Structured carbon nanosheets may reveal a large number of active areas for electrocatalytic processes, according to Tang et al.[78] Similar to the Mo_2C catalysts,[66] ultrafine nanoparticles with an average grain size of 3–5 nm are attached into nanosheets in a high-resolution TEM picture (Figure 6B). Three kinds of lattice plane distances were detected in HRTEM and presented in Figure S4. The first type of lattice plane distance of about ~0.36 nm can be ascribed to the (002) plane in N-doped graphite structure (Figure 4A), the second kind of lattice plane with a distance of ~0.227 nm is in good agreement with the (101) plane of Mo_2C (Figures 5C and S4B), and agrees with XRD data.[39] The last kind with a lattice distance of 0.219 nm correlated with the (211) plane of MoO_2 (Figures 6C and S4C). Based on TEM results, we can conclude that the sample has molybdenum carbide nanoparticles with MoO_2-Mo_2C heterointerfaces embedded into the structure of N-doped graphitic carbon.

Using a three-electrode setup in an Ar-saturated 1M KOH, the HER activities of MGM electrodes for water splitting were investigated. The findings are shown in Figure 7. A step-by-step algorithm was used to conduct electrochemical testing of MGM materials, which included linear sweep voltammetry (LSV), impedance spectroscopy (EIS) and chronopotentiometry (CP). In the first step, LSV measurements were carried out

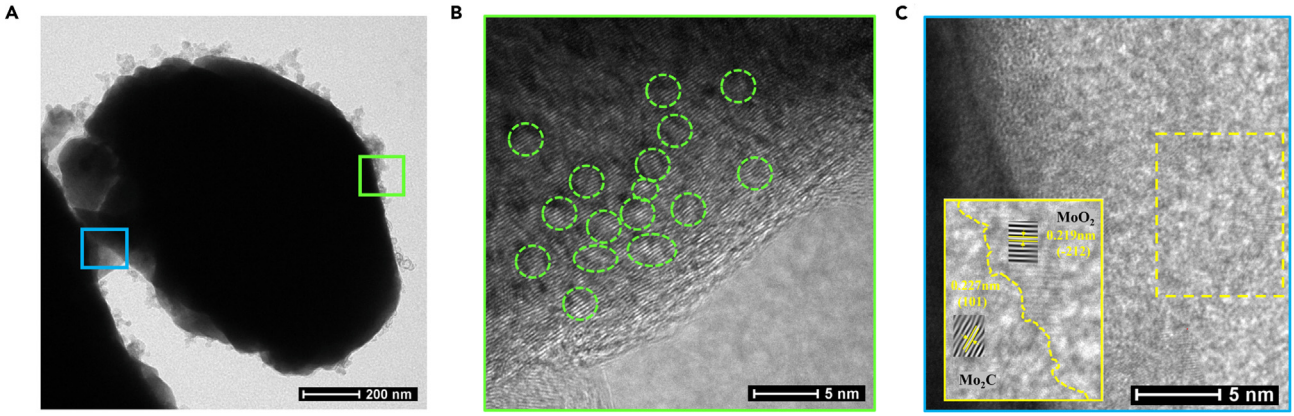

Figure 6. TEM and HRTEM images for MGM-2 samples

(A) TEM.

(B and C) HRTEM images for the MGM-2 sample.

at 1 mV s^{-1} scan rate, as presented in Figure 7A. As shown in Table S3. LSV curves KOH at a scan rate of 1 mVs^{-1} of MGM electrodes and Pt (20%)/C for HER in a 1.0 M after CP test. The onset potential values for MGM-1, MGM-2, MGM-3, and MGM-4 are 51, 58, 68, and 65 mV, respectively. And the overpotential values are 191 and 222 mV for MGM-1, 203 and 233 mV for MGM-2, 259 and 288 mV for MGM-3, 233 and 261 mV for MGM-4 at current densities of 10 and 20 mA cm^{-2}. But at high current densities from 100 to 300 mA cm^{-2}, the potentials are 302 and 377, 299 and 353, 352 and 417, and 327 and 396 mV for MGM-1, MGM-2, MGM-3, and MGM-4, respectively. It can be concluded that the MGM-1 electrode has a smaller overpotential than other MGM samples at current densities of 10 mA cm^{-2}, and the MGM-2 electrode will have a lower overpotential of hydrogen evolution at higher current densities, starting from 75 mA cm^{-2}. In addition, the LSV of the carbon fiber (CF), MoO_2, and commercial Mo_2C were also measured to confirm the good catalytic properties of MGM-1, which are shown in Figure S5. As a reference sample for comparison results, MGM samples used Pt (20%)/C electrode, which has a hydrogen overvoltage allocation order η_{10} = 31 mV at the current density of 10 mA cm^{-2}.

In alkaline conditions, the HER process can be described using the Tafel-Volmer-Heyrovsky mechanism, which is based on three main reactions:

$$H_2O + e^- \rightarrow H_{ads} + OH^- \text{ (Volmer reaction);}$$

$$H_2O + H_{ads} + e^- \rightarrow H_2 + OH^- \text{ (Heyrovsky reaction);}$$

$$H_{ads} + H_{ads} \rightarrow H_2 \text{ (Tafel reaction).}$$

Volmer-Heyrovsky and Volmer-Tafel are the two typical routes that a general reaction can take. The Tafel slope for Volmer reaction, Heyrovsky reaction and Tafel reaction are 120 mV·dec^{-1}, 40 mV·dec^{-1}, and 30 mV·dec^{-1}, respectively. The complete HER process corresponds to the evolution of molecular hydrogen, where HER can occur via the Volmer-Heyrowsky mechanism or the Volmer-Tafel mechanism. Therefore, Tafel slope values were calculated to determine the predominant HER reaction on the catalyst surface in 1M KOH. As shown in Figure 7B, the results indicate the system is in a non-equilibrium state since the lowest Tafel slope corresponds to MGM-3 (93.46 mV·dec^{-1}), but the lowest overpotential corresponds to 191 mV of MGM-1 (111.97 mV·dec^{-1}).

As is well known, determining the electrochemically active surface area (ECSA) by calculating the Helmholtz double layer capacitance (C_{dl}) is one method of electrocatalysis. C_{dl} was measured by cyclic voltammetry in 1M KOH to determine the ECSA of MGM materials. Figure S6 shows CV curves recorded in the potential windows from 0.2 to 0.3 V vs. RHE at a scan rate of 10–100 mV s^{-1}. The C_{dl} values of all electrodes are calculated at half the capacitive slope current depending on the scan speed. The resulting values of MGM-1, MGM-2, MGM-3, and MGM-4 are 57, 82, 35, and 32 mF cm^{-2}, respectively, which correlates with MGM-2 having a high ECSA and is also key to rapid delivery of reagents for favorable HER kinetics.

The polarization resistance of MGM materials in 1M KOH was examined using an electrochemical impedance spectroscopy test, which was performed in the frequency range of 10-2 to 105 Hz with an amplitude of 5 mV s^{-1} at the open circuit potential (Figure S7). All curves on the Nyquist plot are semicircles that agree with the equivalent circuit model as shown in Figure S8. The equivalent circuit includes the following elements: series resistance (R_s), charge transfer resistance (R_{ct}), and constant phase element (CPE).[79] In the high-frequency region, R_s corresponds to the curve intersection of the curve with the z′ axis, which consists of the bulk resistance of the electrolyte and the resistance of the two electrodes. In the mid-frequency region, CPE refers to the charge transfer resistance of the low-frequency region and the capacitance of the Helmholtz double layer (C_{dl}), and the charge transfer resistance (R_{ct}) refers to the internal resistance to charge transfer in the low-frequency region. In the mid-frequency region, CPE corresponds to the internal resistance of the charge transfer resistance of the low-frequency region and the capacitance of the double

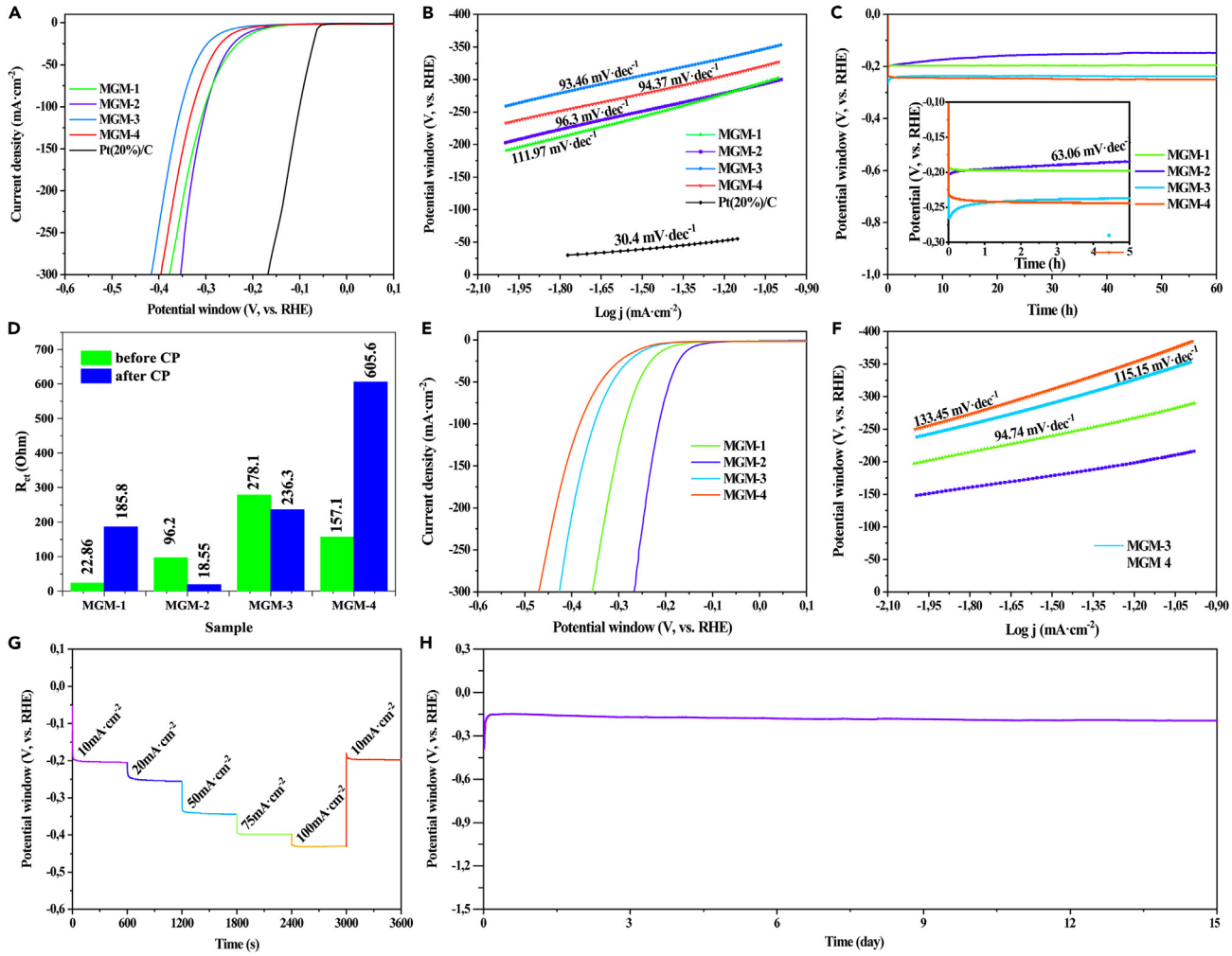

Figure 7. Electrochemical measurements of MGM sample

(A) LSV curves KOH at a scan rate of 1 mVs^{-1} of MGM electrodes and Pt (20%)/C for HER in a 1.0 M.

(B) Calculated Tafel plots.

(C) Time dependence of potential under current density of 10 mA cm^{-2} of MGM electrodes.

(D) Rct values for MGM samples before and after CP test.

(E) LSV curves KOH at a scan rate of 1 mVs^{-1} of MGM electrodes and Pt (20%)/C for HER in a 1.0 M after CP test.

(F) Calculated Tafel plots.

(G) Time dependences of potential at different current densities for MGM-2 electrode.

(H) Test for the long-term stability of the MGM-2 electrode with a fixed current density of 10 mA·cm-2 for a duration of 15 days.

layer (C_{dl}), and in the low-frequency region, the charge transfer resistance (R_{ct}) refers to the internal resistance to charge transfer. It is known that electrochemical activity is inversely proportional to R_{ct}, which ranges from 22.86 to 278.1 Ω. The smallest series resistance R_{ct} belongs to MGM-1, and the largest to MGM-3. The EIS test results correlate very well with the LSV results, which confirm the good catalytic activity of HER for the MGM-1 sample. At the next step, chronopotentiometry CP tests were performed for 60 h at a current of 10 mA cm^{-2}, shown in Figure 7C. Since the system is not in equilibrium, the potential of the MGM-1 sample gradually increases from 191 to 197 mV and reaches a plateau in the first hour, which will last until the end of the CP test. After the first 3.5 h, the potential of the MGM-4 sample gradually increases from 233 to 250 mV and continues to decline to 250 mV during the further test. However, the potential value of the MGM-3 sample decreases from 266 to 238 mV after the next 3 h and remains constant throughout the test. In contrast, the MGM-2 electrode reaches its minimum at 146 mV after 43 h of treatment, but the overpotential tends to increase slightly (148 mV) over the next 17 h. Changes in catalytic activity are reflected in the electrically conductive properties of the MGM samples, as shown in Figure 7D. The Nyquist plots of MGM samples correspond to the equivalent circuit (Figure S8), and suggest that the MGM-2 sample has the smallest charge-transfer resistance (R_{ct}) of 18.55 Ω. Series resistance R_{ct} of MGM-1, MGM-3, and MGM-4 are 185.8, 236.3, and 605.6 Ω, respectively, and exceed the value of MGM-2 (Table S4).

Further, LSV measurements confirmed that the electrocatalytic activity of the MGM-2 electrode improved, as exhibited in Figure 7E. As shown in Table S3. The final overpotential values at current densities of 10 mA cm^{-2} for MGM-1, MGM-2, MGM-3, and MGM-4 are 197 mV, 148 mV, 238 mV, and 250 mV, respectively. Moreover, HER activity has been evaluated by Tafel plots, as illustrated in Figure 7F. The Tafel plot for the MGM-2 sample is 63.06 mV·dec^{-1}, which is lowest than 94.74 mV·dec^{-1} for MGM-1, 115.15 mV·dec^{-1} for MGM-3, and 113.45 mV·dec^{-1} for MGM-4 (Table S3). When compared to several published values for the performance of non-noble metal HER electrocatalysts in alkaline electrolytes, the obtained results show a beneficially low overpotential for the current density of 10 mA cm^{-2} (Table S5), which indicates the positive effect of the ultrasmall size of the Mo_2C and MoO_2 nanoparticles as well as the coupling effect between Mo_2C, MoO_2 and N-doped carbon matrix in the Mo_2C-MoO_2@GC-N catalyst. Moreover, the difference in overpotential values for MGM-1 and MGM-2 clearly correlates with the amount of Mo_2C-MoO_2 heterostructure in the carbon carrier (Table S1). At the same time, samples MGM-3 and MGM-4 than demonstrate similar high overpotential due to the presence of metallic molybdenum, which, when reacting with alkali, is oxidized and converted into a K_2MoO_4 compound on the surface of the carbon matrix, blocking active centers and reducing the rate of charge transfer. Thus, we can formulate a rule for obtaining a highly efficient catalyst with a Mo_2C:MoO_2 heterostructure doped into a carbon support, that the amount of MoO_2 should be at least three times higher than Mo_2C in the absence of metallic Mo.

To evaluate the electrochemical stability of MGM-2 with HER were carried out multi-step chronopotentiometry tests at current densities from 10 to 100 mA cm^{-2} for 1 h (Figure 7G). The current densities are 10, 20, 50, 75, 100 mA cm^{-2} and end at 10 mA cm^{-2} with a step at every 600 s. The produced catalyst exhibits great stability across a broad range of overpotentials, as seen by the overpotential remaining rather steady at every current density across the test range.

Thus, the overpotentials at 10, 20, 50, 75, and 100 mA cm^{-2} are 151, 198, 289, 343, and 374, respectively, and in the last step, the overpotentials decreased to 138 mV after decreasing the current density from 100 to 10 mA cm^{-2}. Additionally, the long-term HER stability test in 1M KOH at 10 mA cm^{-2}, respectively, and at the last step, the overpotentials decreased to 138 mV after decreasing the current density from days indicates once again that the MGM-2 material retains its electrocatalytic activity for a long time, as shown in Figure 7H. Then, the MGM-2 electrode exhibits the stability of HER with a slow rise in the potential to 174 mV for the next 13 days. The obtained values of the long-term HER stability test correspond to an increase in HER potential of only 17% after 15 days. The dissolution of molybdenum on the electrode surface and the opening of more catalytic centers are responsible for the increase in catalytic performance.[58] The gradual increase in the overpotential of HER can be explained by the fact that the amount of molybdenum gradually decreased and the electrocatalyst was a graphite matrix doped with molybdenum remainders.[80]

After the long-term test for 15 days, the MGM-2 electrode was examined by XRD, XPS, and SEM methods to better understand the processes that influenced the reasons for the decrease in catalytic properties. Figure S11 shows the XRD patterns of the MGM-2 sample before and after the long-term stability test. It can be observed that the diffraction profiles have significant differences. A more detailed analysis revealed additional peaks around 26.3° (Figure S11B), 30.5, 33.7, 35.2, 36.8, 39.4, 40.4, 44.8, 46.2, 50.0, and 54.5° (Figure S11C), which assigned to the crystalline phase K_2MoO_4 (ISCD #96-152-7398). The negative shift of the peaks, as well as the change in the intensity of the Mo_2C peaks after long-term testing compared to the standard intensity and position of the peaks, confirms the transformation of the composite.[81] According to XRD, the MGM-2 sample after testing, contained the following crystalline phases: graphite, 94.3% wt.; MoO_2, 3.0 % wt., K_2MoO_4, 2.6 % wt., and Mo_2C, 0.2% wt.

The outcome and the XPS measurements accord fairly well (Figure S12). XPS analysis indicates the presence of only Mo, C, N, O, and K on the surface. Figure S12B displays the high-resolution XPS spectra of Mo3d, the peak fitting indicates that there are another two oxidation states Mo^{4+} and Mo^{6+} for Mo on the surface of MGM-2 after a long-term stability test. The absence of Mo^{2+}oxidation states suggests the disappearance of Mo_2C on the electrode surface, which confirms the XRD results. It should be highlighted that the Mo3d peaks' intensity dramatically dropped, indicating that molybdenum had been removed from the catalyst. In the course of the electrochemical experiment, Mo^{6+} dissolves in an alkaline electrolyte and promotes the opening of additional catalytic centers, which favor the HER processes. It should be noted that under the conditions of the cathodic process, only molybdenum oxide dissolves in the electrolyte, which was oxidized in the air during the synthesis of the catalyst.[58,80] However, some loss of Mo_2C is also possible due to the gradual destruction of the surface through the intense release of gas bubbles. Therefore, the catalyst is a graphite matrix with embedded molybdenum. As illustrated in Figure S12C, the high-resolution C1s spectrum contains three individual peaks for the different types of C atoms, which are ascribed to C=C/C–C, C–O/C–N, and C=O bonds at 284.8, 286.6, and 287.8 eV, respectively. The C–N/C–O bond configurations allow the composites to have higher electrocatalytic activity for HER due to their ability to facilitate proton adsorption and stabilization of reaction intermediates. This results in improved HER performance in terms of lower overvoltages and higher current densities, as seen in Table S3. In addition, the stability of the C–O/C–N bonds under the HER process in alkaline conditions is crucial. Stable bonds ensure the long-term durability of the composite material, maintaining its catalytic activity over extended time. It follows that the graphite matrix doped with nitrogen as a catalyst carrier is stable for a long time, but the catalytic centers undergo transformations, as evidenced by the signals in the Mo_3d and K2p spectra. The K2p spectra are due to the sorption of potassium ions on the surface and the formation of K_2MoO_4 from the 1M KOH electrolyte. The formation of K_2MoO_4 on the Mo_2C surface in the form of a layer or adsorbed particles leads to partial blocking of the active sites of Mo_2C, which reduces the accessibility of active sites and reduces the catalytic activity, which can be observed during very long electrochemical tests. The XPS spectra of N1s could be deconvoluted into four main peaks located at 398.4, 400.3, and ~401.6 eV, corresponding to pyridinic-N, pyrrolic-N, graphitic-N, and Mo3d, respectively, as shown in Figure S12D. The XPS of O1s can be decomposed to the two polynomial peaks (533.7 and 531.9 eV) belonging to the C–O and C=O bonds presented in Figure S12E. SEM image and elementary mapping of MGM-2 after long-term stability tests are shown in Figure S13. It is seen that the morphology of the MGM-2 electrode has changed significantly in comparison with the initial material (Figure 3B). The material became like a sponge with a large number of pores and interspersed with spherical nanoparticles. Carbon and nitrogen

mapping shows that the main material is intertwined carbon nanosheets doped with nitrogen. In addition, molybdenum, potassium, and oxygen are present on the surface (Figure S13). Therefore, molybdenum carbide and oxide are partially converted to K_2MoO_4, which is in good agreement with XRD data. The results of EDS analysis for the MGM-2 sample after the long-term stability test also support this conclusion (Table S6).

Following a protracted HER procedure, the MGM-2 electrode analysis verified that the catalyst's composition and shape had changed. The amount of molybdenum decreases due to dissolution in an alkaline environment. As a result, the final catalyst is a nitrogen-doped graphite matrix with embedded molybdenum. In general, the overpotential of the HER for the formed composites is higher than the values of the initial samples. However, the stability of the synthesized composite catalysts is high, which suggests the possibility of practical use.

Conclusion

In summary, a comprehensive analysis of the properties and structure of MGM powder materials obtained by DC arc plasma was carried out by X-ray diffractometry, scanning microscopy combined with energy dispersive analysis, X-ray photoelectron spectroscopy, and electrochemical methods. The different phase compositions and particle sizes are obtained by changing the proportion of initial components. MGM-2 sample shows the highest and stable electrocatalytic activity for HER with the overpotential of −148 mV to achieve the current density of 10 $mA \cdot cm^{-2}$ and small Tafel slope of 63 $mV \cdot dec^{-1}$ in 1M KOH electrolyte, which corresponds to the close bonding interaction at the atomic level between Mo_2C, MoO_2 and nitrogen-doped carbon species, thereby facilitating the rate of charge transfer. Meanwhile, the electrocatalyst exhibits good long-term electrochemical durability for 15 days. The final stable catalyst was found to be a carbon matrix doped with molybdenum and nitrogen. It can be argued that on the basis of the work presented enriched our knowledge in the field of design and development of catalytically active matter of the Mo-C type for hydrogen production.

Limitation of the study

Our work demonstrates the synthesis of Mo_2C-MoO_2@GC-N heterostructures via the ambient DC arc plasma method for efficient hydrogen production in alkaline electrolyte. However, the mechanism for the opening of additional active sites and the subsequent dissolution of molybdenum in the electrolyte during catalyst operation remains to be studied in order to find an effective way to prevent degradation during catalyst operation. This will be the focus of our future research.

STAR★METHODS

Detailed methods are provided in the online version of this paper and include the following:

- KEY RESOURCES TABLE
- RESOURCE AVAILABILITY
  - Lead contact
  - Materials availability
  - Data and code availability
- METHOD DETAILS
  - Material and synthesis
  - Material characterizations
  - Preparation and electrochemical tests

SUPPLEMENTAL INFORMATION

Supplemental information can be found online at https://doi.org/10.1016/j.isci.2024.110551.

ACKNOWLEDGMENTS

This research was supported by TPU development program.

Funding

The study was supported by the Ministry of Science and Higher Education of the Russian Federation (project no. FSWW-2022-0018).

AUTHOR CONTRIBUTIONS

M.C.: writing – review & editing, writing – original draft, software, methodology, and formal analysis. Y.Z.V.: writing – original draft, validation, and conceptualization. X.Z.: writing – original draft, resources, and conceptualization. S.L.: visualization and software. A.Y.P.: supervision, project administration, and funding acquisition. W.H.: supervision and funding acquisition.

DECLARATION OF INTERESTS

The authors declare no competing interests.

Received: January 6, 2024
Revised: May 2, 2024
Accepted: July 16, 2024
Published: July 20, 2024

REFERENCES

1. Lewis, N.S., and Nocera, D.G. (2006). Powering the planet: Chemical challenges in solar energy utilization. Proc. Natl. Acad. Sci. USA *103*, 15729–15735. https://doi.org/10.1073/pnas.0603395103.
2. Wang, S., Wang, Y., Zang, S.-Q., and Lou, X.W.D. (2020). Hierarchical Hollow Heterostructures for Photocatalytic CO2 Reduction and Water Splitting. Small Methods *4*, 1900586. https://doi.org/10.1002/smtd.201900586.
3. Wang, X., Gao, W., Zhao, Z., Zhao, L., Claverie, J.P., Zhang, X., Wang, J., Liu, H., and Sang, Y. (2019). Efficient photo-electrochemical water splitting based on hematite nanorods doped with phosphorus. Appl. Catal. B Environ. *248*, 388–393. https://doi.org/10.1016/j.apcatb.2019.02.048.
4. Tang, J., Zhou, W., Guo, R., Huang, C., Pan, W., and Liu, P. (2019). An exploration on in-situ synthesis of europium doped g-C3N4 for photocatalytic water splitting. Energy Proc. *158*, 1553–1558. https://doi.org/10.1016/j.egypro.2019.01.365.
5. Upadhyay, S., and Pandey, O.P. (2020). One-pot synthesis of pure phase molybdenum carbide (Mo2C and MoC) nanoparticles for hydrogen evolution reaction. Int. J. Hydrogen Energy *45*, 27114–27128. https://doi.org/10.1016/j.ijhydene.2020.07.069.
6. Wang, J.-Y., Ouyang, T., Deng, Y.-P., Hong, Y.-S., and Liu, Z.-Q. (2019). Metallic Mo2C anchored pyrrolic-N induced N-CNTs/NiS2 for efficient overall water electrolysis. J. Power Sources *420*, 108–117. https://doi.org/10.1016/j.jpowsour.2019.02.098.
7. Mu, C., Butenko, D.S., Odynets, I.V., Zatovsky, I.V., Li, J., Han, W., and Klyui, N.I. (2020). Na4Ni3P4O15–Ni(OH)2 core–shell nanoparticles as hybrid electrocatalysts for the oxygen evolution reaction in alkaline electrolytes. Dalton Trans. *49*, 8226–8237. https://doi.org/10.1039/D0DT01205J.
8. McKone, J.R., Warren, E.L., Bierman, M.J., Boettcher, S.W., Brunschwig, B.S., Lewis, N.S., and Gray, H.B. (2011). Evaluation of Pt, Ni, and Ni–Mo electrocatalysts for hydrogen evolution on crystalline Si electrodes. Energy Environ. Sci. *4*, 3573–3583. https://doi.org/10.1039/C1EE01488A.
9. Butenko, D.S., Li, S., Kotsyubynsky, V.O., Boychuk, V.M., Dubinko, V.I., Kolkovsky, P.I., Liedienov, N.A., Klyui, N.I., Han, W., and Zatovsky, I.V. (2021). Palladium nanoparticles embedded in microporous carbon as electrocatalysts for water splitting in alkaline media. Int. J. Hydrogen Energy *46*, 21462–21474. https://doi.org/10.1016/j.ijhydene.2021.03.242.
10. Youn, D.H., Han, S., Kim, J.Y., Kim, J.Y., Park, H., Choi, S.H., and Lee, J.S. (2014). Highly Active and Stable Hydrogen Evolution Electrocatalysts Based on Molybdenum Compounds on Carbon Nanotube–Graphene Hybrid Support. ACS Nano *8*, 5164–5173. https://doi.org/10.1021/nn5012144.
11. Mu, Y., Zhang, Y., Fang, L., Liu, L., Zhang, H., and Wang, Y. (2016). Controllable synthesis of molybdenum carbide nanoparticles embedded in porous graphitized carbon matrixes as efficient electrocatalyst for hydrogen evolution reaction. Electrochim. Acta *215*, 357–365. https://doi.org/10.1016/j.electacta.2016.08.104.
12. Ma, Y., Guan, G., Hao, X., Cao, J., and Abudula, A. (2017). Molybdenum carbide as alternative catalyst for hydrogen production – A review. Renew. Sustain. Energy Rev. *75*, 1101–1129. https://doi.org/10.1016/j.rser.2016.11.092.
13. Yin, J., Fan, Q., Li, Y., Cheng, F., Zhou, P., Xi, P., and Sun, S. (2016). Ni–C–N Nanosheets as Catalyst for Hydrogen Evolution Reaction. J. Am. Chem. Soc. *138*, 14546–14549. https://doi.org/10.1021/jacs.6b09351.
14. Gong, S., Jiang, Z., Shi, P., Fan, J., Xu, Q., and Min, Y. (2018). Noble-metal-free heterostructure for efficient hydrogen evolution in visible region: Molybdenum nitride/ultrathin graphitic carbon nitride. Appl. Catal. B Environ. *238*, 318–327. https://doi.org/10.1016/j.apcatb.2018.07.040.
15. Vrubel, H., and Hu, X. (2012). Molybdenum Boride and Carbide Catalyze Hydrogen Evolution in both Acidic and Basic Solutions. Angew. Chem. Int. Ed. Engl. *51*, 12703–12706. https://doi.org/10.1002/anie.201207111.
16. Ma, Y.-Y., Wu, C.-X., Feng, X.-J., Tan, H.-Q., Yan, L.-K., Liu, Y., Kang, Z.-H., Wang, E.-B., and Li, Y.-G. (2017). Highly efficient hydrogen evolution from seawater by a low-cost and stable CoMoP@C electrocatalyst superior to Pt/C. Energy Environ. Sci. *10*, 788–798. https://doi.org/10.1039/C6EE03768B.
17. Feng, L.-L., Yu, G., Wu, Y., Li, G.-D., Li, H., Sun, Y., Asefa, T., Chen, W., and Zou, X. (2015). High-Index Faceted Ni3S2 Nanosheet Arrays as Highly Active and Ultrastable Electrocatalysts for Water Splitting. J. Am. Chem. Soc. *137*, 14023–14026. https://doi.org/10.1021/jacs.5b08186.
18. Zhang, L., Hu, Z., Huang, J., Chen, Z., Li, X., Feng, Z., Yang, H., Huang, S., and Luo, R. (2022). Experimental and DFT studies of flower-like Ni-doped Mo2C on carbon fiber paper: A highly efficient and robust HER electrocatalyst modulated by Ni(NO3)2 concentration. J. Adv. Ceram. *11*, 1294–1306. https://doi.org/10.1007/s40145-022-0610-6.
19. Zhang, L., Huang, J., Hu, Z., Li, X., Ding, T., Hou, X., Chen, Z., Ye, Z., and Luo, R. (2022). Ni(NO3)2-induced high electrocatalytic hydrogen evolution performance of self-supported fold-like WC coating on carbon fiber paper prepared through molten salt method. Electrochim. Acta *422*, 140553. https://doi.org/10.1016/j.electacta.2022.140553.
20. Xiao, P., Yan, Y., Ge, X., Liu, Z., Wang, J.-Y., and Wang, X. (2014). Investigation of molybdenum carbide nano-rod as an efficient and durable electrocatalyst for hydrogen evolution in acidic and alkaline media. Appl. Catal. B Environ. *154–155*, 232–237. https://doi.org/10.1016/j.apcatb.2014.02.020.
21. Zhang, S., Wang, C., Qiu, H., Bao, Y., Long, T., Cai, W., and Huang, Y. (2020). Highly graphitic carbon shell on molybdenum carbide nanosheets by iron doping for stable hydrogen evolution. Int. J. Hydrogen Energy *45*, 14368–14374. https://doi.org/10.1016/j.ijhydene.2020.03.182.
22. Liu, B., Wang, S., Mo, Q., Peng, L., Cao, S., Wang, J., Wu, C., Li, C., Guo, J., Liu, B., et al. (2018). Epitaxial MoS2 nanosheets on nitrogen doped graphite foam as a 3D electrode for highly efficient electrochemical hydrogen evolution. Electrochim. Acta *292*, 407–418. https://doi.org/10.1016/j.electacta.2018.09.160.
23. Gao, H., Yao, Z., Shi, Y., Jia, R., Liang, F., Sun, Y., Mao, W., and Wang, H. (2018). Simple and large-scale synthesis of β-phase molybdenum carbides as highly stable catalysts for dry reforming of methane. Inorg. Chem. Front. *5*, 90–99. https://doi.org/10.1039/C7QI00532F.
24. Wu, C., and Li, J. (2017). Unique Hierarchical Mo2C/C Nanosheet Hybrids as Active Electrocatalyst for Hydrogen Evolution Reaction. ACS Appl. Mater. Interfaces *9*, 41314–41322. https://doi.org/10.1021/acsami.7b13822.
25. Xing, J., Li, Y., Guo, S., Jin, T., Li, H., Wang, Y., and Jiao, L. (2019). Molybdenum carbide in-situ embedded into carbon nanosheets as efficient bifunctional electrocatalysts for overall water splitting. Electrochim. Acta *298*, 305–312. https://doi.org/10.1016/j.electacta.2018.12.091.
26. Zhang, K., Li, C., Zhao, Y., Yu, X., and Chen, Y. (2015). Porous one-dimensional Mo2C–amorphous carbon composites: high-efficient and durable electrocatalysts for hydrogen generation. Phys. Chem. Chem. Phys. *17*, 16609–16614. https://doi.org/10.1039/C5CP02028J.
27. Huang, Y., Wang, C., Song, H., Bao, Y., and Lei, X. (2018). Carbon-coated molybdenum carbide nanosheets derived from molybdenum disulfide for hydrogen evolution reaction. Int. J. Hydrogen Energy *43*, 12610–12617. https://doi.org/10.1016/j.ijhydene.2018.03.233.
28. Wu, S., Chen, M., Wang, W., Zhou, J., Tang, X., Zhou, D., and Liu, C. (2021). Molybdenum carbide nanoparticles assembling in diverse heteroatoms doped carbon matrix as efficient hydrogen evolution electrocatalysts in acidic and alkaline medium. Carbon *171*, 385–394. https://doi.org/10.1016/j.carbon.2020.09.037.
29. Li, J.-S., Wang, Y., Liu, C.-H., Li, S.-L., Wang, Y.-G., Dong, L.-Z., Dai, Z.-H., Li, Y.-F., and Lan, Y.-Q. (2016). Coupled molybdenum carbide and reduced graphene oxide electrocatalysts for efficient hydrogen evolution. Nat. Commun. *7*, 11204. https://doi.org/10.1038/ncomms11204.
30. Jing, S., Zhang, L., Luo, L., Lu, J., Yin, S., Shen, P.K., and Tsiakaras, P. (2018). N-Doped Porous Molybdenum Carbide Nanobelts as Efficient Catalysts for Hydrogen Evolution Reaction. Appl. Catal. B Environ. *224*, 533–540. https://doi.org/10.1016/j.apcatb.2017.10.025.

31. Cao, Q., Zhao, L., Wang, A., Yang, L., Lai, L., Wang, Z.-L., Kim, J., Zhou, W., Yamauchi, Y., and Lin, J. (2019). Tailored synthesis of Zn–N co-doped porous MoC nanosheets towards efficient hydrogen evolution. Nanoscale *11*, 1700–1709. https://doi.org/10.1039/C8NR07463A.
32. Wan, C., and Leonard, B.M. (2015). Iron-Doped Molybdenum Carbide Catalyst with High Activity and Stability for the Hydrogen Evolution Reaction. Chem. Mater. *27*, 4281–4288. https://doi.org/10.1021/acs.chemmater.5b00621.
33. Gómez–Marín, A.M., and Ticianelli, E.A. (2017). Effect of transition metals in the hydrogen evolution electrocatalytic activity of molybdenum carbide. Appl. Catal. B Environ. *209*, 600–610. https://doi.org/10.1016/j.apcatb.2017.03.044.
34. Wang, S., Bendt, G., Saddeler, S., and Schulz, S. (2019). Synergistic Effects of Mo2C-NC@CoxFey Core–Shell Nanoparticles in Electrocatalytic Overall Water Splitting Reaction. Energy Tech. *7*, 1801121. https://doi.org/10.1002/ente.201801121.
35. Mohammed-Ibrahim, J., and Sun, X. (2019). Recent progress on earth abundant electrocatalysts for hydrogen evolution reaction (HER) in alkaline medium to achieve efficient water splitting – A review. J. Energy Chem. *34*, 111–160. https://doi.org/10.1016/j.jechem.2018.09.016.
36. Lee, G.H., Lee, M.H., Kim, Y., Lim, H.-K., and Youn, D.H. (2019). Facile synthesis of nanostructured molybdenum carbide/nitrogen-doped CNT-RGO composite via a modified urea glass route for efficient hydrogen evolution. J. Alloys Compd. *805*, 113–119. https://doi.org/10.1016/j.jallcom.2019.06.355.
37. Liu, M., Yang, Y., Luan, X., Dai, X., Zhang, X., Yong, J., Qiao, H., Zhao, H., Song, W., and Huang, X. (2018). Interface-Synergistically Enhanced Acidic, Neutral, and Alkaline Hydrogen Evolution Reaction over Mo2C/MoO2 Heteronanorods. ACS Sustain. Chem. Eng. *6*, 14356–14364. https://doi.org/10.1021/acssuschemeng.8b03026.
38. Ni, J., Ruan, Z., Zhu, S., Kan, X., Lu, L., and Liu, Y. (2019). Sandwiched NiO/β-Mo2C/RGO as Improved Electrocatalyst for Hydrogen Evolution Reaction: Solvothermal-Assisted Self-Assembly and Catalytic Mechanism. Chemelectrochem *6*, 5958–5966. https://doi.org/10.1002/celc.201901646.
39. He, L., Zhang, W., Mo, Q., Huang, W., Yang, L., and Gao, Q. (2020). Molybdenum Carbide-Oxide Heterostructures: In Situ Surface Reconfiguration toward Efficient Electrocatalytic Hydrogen Evolution. Angew. Chem. Int. Ed. Engl. *59*, 3544–3548. https://doi.org/10.1002/anie.201914752.
40. Chen, W.-F., Iyer, S., Iyer, S., Sasaki, K., Wang, C.-H., Zhu, Y., Muckerman, J.T., and Fujita, E. (2013). Biomass-derived electrocatalytic composites for hydrogen evolution. Energy Environ. Sci. *6*, 1818–1826. https://doi.org/10.1039/C3EE40596F.
41. Cui, W., Cheng, N., Liu, Q., Ge, C., Asiri, A.M., and Sun, X. (2014). Mo2C Nanoparticles Decorated Graphitic Carbon Sheets: Biopolymer-Derived Solid-State Synthesis and Application as an Efficient Electrocatalyst for Hydrogen Generation. ACS Catal. *4*, 2658–2661. https://doi.org/10.1021/cs5005294.
42. Zhang, X., Wang, J., Guo, T., Liu, T., Wu, Z., Cavallo, L., Cao, Z., and Wang, D. (2019). Structure and phase regulation in MoxC (α-MoC1-x/β-Mo2C) to enhance hydrogen evolution. Appl. Catal. B Environ. *247*, 78–85. https://doi.org/10.1016/j.apcatb.2019.01.086.
43. Jiang, R., Fan, J., Hu, L., Dou, Y., Mao, X., and Wang, D. (2018). Electrochemically synthesized N-doped molybdenum carbide nanoparticles for efficient catalysis of hydrogen evolution reaction. Electrochim. Acta *261*, 578–587. https://doi.org/10.1016/j.electacta.2017.12.174.
44. Liu, J., Hodes, G., Yan, J., and Liu, S.F. (2021). Metal-doped Mo2C (metal = Fe, Co, Ni, Cu) as catalysts on TiO2 for photocatalytic hydrogen evolution in neutral solution. Chin. J. Catal. *42*, 205–216. https://doi.org/10.1016/S1872-2067(20)63589-6.
45. Khabbaz, S., Honarbakhsh-Raouf, A., Ataie, A., and Saghafi, M. (2013). Effect of processing parameters on the mechanochemical synthesis of nanocrystalline molybdenum carbide. Int. J. Refract. Metals Hard Mater. *41*, 402–407. https://doi.org/10.1016/j.ijrmhm.2013.05.014.
46. Tao, Y., Zhu, S., Pan, Z., Qiu, S., and Shen, X. (2019). Preparation and process investigation of molybdenum carbide and their N-doped analogue by calcination. J. Solid State Chem. *280*, 120961. https://doi.org/10.1016/j.jssc.2019.120961.
47. Schaidle, J.A., Schweitzer, N.M., Ajenifujah, O.T., and Thompson, L.T. (2012). On the preparation of molybdenum carbide-supported metal catalysts. J. Catal. *289*, 210–217. https://doi.org/10.1016/j.jcat.2012.02.012.
48. Cai, Z., Wang, F., Zhang, X., Ahishakiye, R., Xie, Y., and Shen, Y. (2017). Selective hydrodeoxygenation of guaiacol to phenolics over activated carbon supported molybdenum catalysts. Mol. Catal. *441*, 28–34. https://doi.org/10.1016/j.mcat.2017.07.024.
49. Madrigal-Camacho, M., Vilchis-Nestor, A.R., Camacho-López, M., and Camacho-López, M.A. (2018). Synthesis of MoC@Graphite NPs by short and ultra-short pulses laser ablation in toluene under N2 atmosphere. Diam. Relat. Mater. *82*, 63–69. https://doi.org/10.1016/j.diamond.2017.12.019.
50. Yosida, Y., and Oguro, I. (2006). Superconductivity in a high-temperature cubic phase of MoCx encapsulated in the multiwall carbon nanocages. Phys. C Supercond. *442*, 97–100. https://doi.org/10.1016/j.physc.2006.04.092.
51. Saito, Y., Matsumoto, T., and Nishikubo, K. (1997). Encapsulation of carbides of chromium, molybdenum and tungsten in carbon nanocapsules by arc discharge. J. Cryst. Growth *172*, 163–170. https://doi.org/10.1016/S0022-0248(96)00709-9.
52. Schur, D.V., Dubovoy, A.G., Zaginaichenko, S.Y., Adejev, V.M., Kotko, A.V., Bogolepov, V.A., Savenko, A.F., and Zolotarenko, A.D. (2007). Production of carbon nanostructures by arc synthesis in the liquid phase. Carbon *45*, 1322–1329. https://doi.org/10.1016/j.carbon.2007.01.017.
53. Wu, H.B., Xia, B.Y., Yu, L., Yu, X.-Y., and Lou, X.W.D. (2015). Porous molybdenum carbide nano-octahedrons synthesized via confined carburization in metal-organic frameworks for efficient hydrogen production. Nat. Commun. *6*, 6512. https://doi.org/10.1038/ncomms7512.
54. Pak, A., Ivashutenko, A., Zakharova, A., and Vassilyeva, Y. (2020). Cubic SiC nanowire synthesis by DC arc discharge under ambient air conditions. Surf. Coating. Technol. *387*, 125554. https://doi.org/10.1016/j.surfcoat.2020.125554.
55. Pak, A., Shanenkov, I.I., Mamontov, G.Y., and Kokorina, A.I. (2020). Vacuumless synthesis of tungsten carbide in a self-shielding atmospheric plasma of DC arc discharge. Int. J. Refract. Metals Hard Mater. *93*, 105343. https://doi.org/10.1016/j.ijrmhm.2020.105343.
56. Pak, A.Y. (2019). The Possibility of Synthesizing Nanosize Molybdenum Carbide in Atmospheric Electrodischarge Plasma. Tech. Phys. Lett. *45*, 866–869. https://doi.org/10.1134/S1063785019090098.
57. Pak, A.Y., Yakich, T.Y., Mamontov, G.Y., Rudmin, M.A., and Vasil'eva, Y.Z. (2020). Obtaining Titanium Carbide in an Atmospheric Electric Discharge Plasma. Tech. Phys. *65*, 771–776. https://doi.org/10.1134/S1063784220050205.
58. Vassilyeva, Y.Z., Butenko, D.S., Li, S., Han, W., and Pak, A.Y. (2020). Synthesis of molybdenum carbide catalyst by DC arc plasma in ambient air for hydrogen evolution. Mater. Chem. Phys. *254*, 123509. https://doi.org/10.1016/j.matchemphys.2020.123509.
59. Shanenkov, I., Nikitin, D., Ivashutenko, A., Shanenkova, Y., Vympina, Y., Butenko, D., Han, W., and Sivkov, A. (2021). Studies on the thermal stability of nanosized powder of WC1-x-based product prepared by plasma dynamic method, compaction feasibility of the powder and preparation of composite with aluminium. Ceram. Int. *47*, 6884–6895. https://doi.org/10.1016/j.ceramint.2020.11.035.
60. Wei, H., Xi, Q., Chen, X., Guo, D., Ding, F., Yang, Z., Wang, S., Li, J., and Huang, S. (2018). Molybdenum Carbide Nanoparticles Coated into the Graphene Wrapping N-Doped Porous Carbon Microspheres for Highly Efficient Electrocatalytic Hydrogen Evolution Both in Acidic and Alkaline Media. Adv. Sci. *5*, 1700733. https://doi.org/10.1002/advs.201700733.
61. Guardia-Valenzuela, J., Bertarelli, A., Carra, F., Mariani, N., Bizzaro, S., and Arenal, R. (2018). Development and properties of high thermal conductivity molybdenum carbide - graphite composites. Carbon *135*, 72–84. https://doi.org/10.1016/j.carbon.2018.04.010.
62. Xia, K., Guo, J., Xuan, C., Huang, T., Deng, Z., Chen, L., and Wang, D. (2019). Ultrafine molybdenum carbide nanoparticles supported on nitrogen doped carbon nanosheets for hydrogen evolution reaction. Chin. Chem. Lett. *30*, 192–196. https://doi.org/10.1016/j.cclet.2018.05.009.
63. Fayos, J. (1999). Possible 3D Carbon Structures as Progressive Intermediates in Graphite to Diamond Phase Transition. J. Solid State Chem. *148*, 278–285. https://doi.org/10.1006/jssc.1999.8448.
64. Zhao, Q., and Kulik, H.J. (2018). Where Does the Density Localize in the Solid State? Divergent Behavior for Hybrids and DFT+U. J. Chem. Theory Comput. *14*, 670–683. https://doi.org/10.1021/acs.jctc.7b01061.
65. Wyckoff, R.W.G. (1935). The structure of crystals : supplement for 1930-1934 to the second edition.
66. Bernuy-Lopez, C., Allix, M., Bridges, C.A., Claridge, J.B., and Rosseinsky, M.J. (2007). Sr2MgMoO6-δ: Structure, Phase Stability, and Cation Site Order Control of Reduction.

Chem. Mater. *19*, 1035–1043. https://doi.org/10.1021/cm0624116.

67. Visser, J.W., and Wolff, P.M. (1964). T.N.O. Absolute intensities e outline of a recommended practice, Report 641.109.
68. Jin, Y., and Shen, P.K. (2015). Nanoflower-like metallic conductive MoO2 as a high-performance non-precious metal electrocatalyst for the hydrogen evolution reaction. J. Mater. Chem. A Mater. *3*, 20080–20085. https://doi.org/10.1039/C5TA06018D.
69. Hu, H., Tian, M., Li, F., Gao, L., Xu, N., Hu, Y., Long, X., Ma, J., and Jin, J. (2018). Phosphorus Dual-Doped MoO2 Nanosheet/Multiwalled Carbon Nanotube Hybrid as Efficient Electrocatalyst for Hydrogen Evolution. Chemelectrochem *5*, 2660–2665. https://doi.org/10.1002/celc.201800829.
70. Yuan, S., Xu, S., Liu, Z., Huang, G., Zhang, C., Ai, J., Li, X., and Li, N. (2019). Ultra-Small Molybdenum Carbide Nanoparticles in situ Entrapped in Mesoporous Carbon Spheres as Efficient Catalysts for Hydrogen Evolution. ChemCatChem *11*, 2643–2648. https://doi.org/10.1002/cctc.201900324.
71. Li, R., Wang, S., Wang, W., and Cao, M. (2015). Ultrafine Mo2C nanoparticles encapsulated in N-doped carbon nanofibers with enhanced lithium storage performance. Phys. Chem. Chem. Phys. *17*, 24803–24809. https://doi.org/10.1039/C5CP03890A.
72. Luo, Y., Jin, C., Wang, Z., Wei, M., Yang, C., Yang, R., Chen, Y., and Liu, M. (2017). A high-performance oxygen electrode for Li–O2 batteries: Mo2C nanoparticles grown on carbon fibers. J. Mater. Chem. A Mater. *5*, 5690–5695. https://doi.org/10.1039/C7TA01249G.
73. Butenko, D.S., Li, S., Chen, R., Odynets, I.V., Li, D., Yuan, Z., Zhang, X., and Zatovsky, I. (2022). Na4Co3P4O15 in situ transformation to Co(OH)2/CoO(OH) nanoforms for aqueous supercapacitor using redox additive electrolyte. Mater. Sci. Eng., B *286*, 116051. https://doi.org/10.1016/j.mseb.2022.116051.
74. Butenko, D.S., Zhang, X., Zatovsky, I.V., Fesych, I.V., Li, S., Chen, R., Chufarov, M., Symonenko, O., Klyui, N.I., and Han, W. (2020). Bi(nanoparticles)/CNx(nanosheets) nanocomposites as high capacity and stable electrode materials for supercapacitors: the role of urea. Dalton Trans. *49*, 12197–12209. https://doi.org/10.1039/D0DT02073G.
75. Jiang, H., Wu, X., Zhang, H., Yan, Q., Li, H., Ma, T., and Yang, S. (2023). Toward effective electrocatalytic C–N coupling for the synthesis of organic nitrogenous compounds using CO2 and biomass as carbon sources. SusMat *3*, 781–820. https://doi.org/10.1002/sus2.175.
76. Zhang, X., Liu, Y., Ma, X., Liu, X., Zhang, R., and Wang, Y. (2023). Metal–Support Interaction of Carbon–Based Electrocatalysts for Oxygen Evolution Reaction. Nanoenergy Advances *3*, 48–72. https://doi.org/10.3390/nanoenergyadv3010004.
77. Liu, C.-H., Tang, Y.-J., Wang, X.-L., Huang, W., Li, S.-L., Dong, L.-Z., and Lan, Y.-Q. (2016). Highly active Co–Mo–C/NRGO composite as an efficient oxygen electrode for water–oxygen redox cycle. J. Mater. Chem. A Mater. *4*, 18100–18106. https://doi.org/10.1039/C6TA07952K.
78. Tang, C., Hu, Q., Li, F., He, C., Chai, X., Zhu, C., Liu, J., Zhang, Q., Zhu, B., and Fan, L. (2018). Coupled molybdenum carbide and nitride on carbon nanosheets: An efficient and durable hydrogen evolution electrocatalyst in both acid and alkaline media. Electrochim. Acta *280*, 323–331. https://doi.org/10.1016/j.electacta.2018.05.129.
79. Yan, Y., Lin, J., Xu, T., Liu, B., Huang, K., Qiao, L., Liu, S., Cao, J., Jun, S.C., Yamauchi, Y., and Qi, J. (2022). Atomic-Level Platinum Filling into Ni-Vacancies of Dual-Deficient NiO for Boosting Electrocatalytic Hydrogen Evolution. Adv. Energy Mater. *12*, 2200434. https://doi.org/10.1002/aenm.202200434.
80. Li, Y., Wei, X., Chen, L., Shi, J., and He, M. (2019). Nickel-molybdenum nitride nanoplate electrocatalysts for concurrent electrolytic hydrogen and formate productions. Nat. Commun. *10*, 5335. https://doi.org/10.1038/s41467-019-13375-z.
81. Yan, Y., Lin, J., Huang, K., Zheng, X., Qiao, L., Liu, S., Cao, J., Jun, S.C., Yamauchi, Y., and Qi, J. (2023). Tensile Strain-Mediated Spinel Ferrites Enable Superior Oxygen Evolution Activity. J. Am. Chem. Soc. *145*, 24218–24229. https://doi.org/10.1021/jacs.3c08598.

STAR★METHODS

KEY RESOURCES TABLE

REAGENT or RESOURCE	SOURCE	IDENTIFIER
Chemicals, peptides, and recombinant proteins		
Mo_2C	Stellite	12069-89-5
MoO_3	Stellite	1313-99-1
MoO_2	Stellite	18868-43-4
C	Heepani Tools Store	1274-68-4
Melamine	Sinopharm	3011-25-28
KOH	Aladdin	1310-58-3
N-methylpyrrolidone	Macklin	872-50-4
PVDF	Dodochem	HSV900
SP	Aladdin	1692-60-7

RESOURCE AVAILABILITY

Lead contact

Further information and requests for resources and reagents should be directed to and will be fulfilled by the lead contact, Wei Han (whan@jlu.edu.cn).

Materials availability

All materials generated in this study are available from the lead contact without restriction.

Data and code availability

- The datasets and images generated during this study are available from the lead contact upon request
- This paper does not report original code.
- Any additional information required to reanalyze the data reported in this paper is available from the lead contact upon request.

METHOD DETAILS

Material and synthesis

Without any additional purification, all reagents were used exactly as supplied. Commercial Mo with 99.95% nominal purity and 1–3 μm particle size, graphite (99.98% purity) and melamine (99.8% purity) powders served as the starting materials. The raw ingredients were precisely weighed and subjected to intense milling at different intervals in a planetary ball mill. The total amount of the initial mixture was 500 ± 50 mg. Four experiments were carried out with different ratios of starting materials in each (Table). The samples were labeled as MGM-X, where X is the sample number. The MGM powders were synthesized via DC arc discharge plasma in an open-air atmosphere using the procedure and setup described earlier.[58] Wherein the synthesis time and the gap between electrodes were the same in each experiment and equal to 10 ± 0.02 s and 0.5 ± 0.1 mm, respectively.

Table. Synthesis parameters

	Initial weight ratio					
Sample	Mo	Graphite	Melamine	Mo/Graphite	Graphite/Melamine	Mo/(Graphite + Melamine)
MGM-1	1.0	3.77	1.89	0.27	2.0	0.18
MGM-2	1.0	2.0	1.0	0.5	2.0	0.33
MGM-3	1.0	0.66	0.34	1.5	2.0	1.0
MGM-4	1.0	0.5	0.5	2	1.0	1.0

The production of the samples did not include the use of any kind of catalyst. Following arcing, the resultant product was extracted without treatment from the cathode surface in preparation for further examinations.

Material characterizations

X-ray diffraction was used to characterize the samples as-prepared. (XRD, DX-2700B diffractometer ($\lambda_{CuK\alpha1}$ = 1.54056 Å, $\lambda_{CuK\alpha2}$ = 1.54439 Å)). The morphology and microstructure were observed by scanning electron microscopy (SEM, Magellan 400 with an Oxford X-Max microanalysis EDS system) and by transmission electron microscopy (TEM, Tecnai G2 F20 S-TWIN). The X-ray photoelectron spectroscopy was recorded to determine the chemical bonding states (XPS, VG ESCALAB MK II). The surface area is measured using BET analysis (Brunauer–Emmett–Teller (BET) theory), which is carried out on a JW-BK132F analyzer by the nitrogen adsorption-desorption measurements of the samples.

Preparation and electrochemical tests

The working electrodes with MGM powders and the benchmark Pt (20%)/C electrode were prepared by applying slurry onto a carbon fiber (CF) (HCP331N), the preparation of which consisted of two stages: 1) a homogeneous mixture of electrocatalyst powder (30 mg), conductive carbon black (3.5 mg) and polyvinylidene fluoride was prepared (1.75 mg); 2) N-methylpyrrolidone was added in portions to achieve a creamy suspension. In this case, the working surface of the electrodes was 1cm^2 with a size of 2 × 1 cm, which was dried in a vacuum drying oven at 60°C for 24 h.

The electrochemical tests were performed by the electrochemical workstation (CHI 760E, Shanghai, China) with three-electrode cell in 1M KOH electrolyte (pH = 14). A commercial Hg/HgO electrode and a platinum plate were used as the reference electrode and counter electrode, respectively. For all electrochemical measurements, all measured potentials vs. Hg/HgO were calculated to vs. Reversible Hydrogen Electrode (RHE): ($E_{RHE} = E_{Hg/HgO} + 0.098 + 0.059 \times pH$). The electrochemical impedance spectroscopy (EIS) was collected with an amplitude of 5 mV at the open circuit potential in the frequency of 0.1–100 kHz. The linear sweep voltammetry (LSV) curves toward HER were tested with iR-compensation at a scan rate of 1 mV s^{-1} (iR-compensation applied before LSV measurements). Chronopotentiometry (CP) tests were performed under a constant current density of 10 mA cm^{-2} and at different current densities in the range from 100 to 500 mA cm^{-2} for 50 h and 2 weeks, respectively.